Test of the He-McKellar-Wilkens topological phase by atom interferometry. II. The experiment and its results

S. Lepoutre, J. Gillot, A. Gauguet, M. Büchner, and J. Vigué*
Laboratoire Collisions Agrégats Réactivité–IRSAMC, Université de Toulouse–UPS and CNRS UMR 5589
118, Route de Narbonne, 31062 Toulouse Cedex, France
(Received 12 June 2013; published 21 October 2013)

In this paper, we describe an experimental test of the He-McKellar-Wilkens (HMW) topological phase with our lithium atom interferometer. The expected value of the HMW phase shift in our experiment is small and its measurement was difficult because of stray phase shifts due to small experimental defects. We start by describing our setup and we characterize the effects of the electric and magnetic fields needed to observe the HMW effect. Then we develop a model of our interferometer signals including all the defects we have identified. After various tests of this model, we use it to suppress the majority of the stray phase shifts. We thus obtain a series of measurements of the HMW phase: the results are 31% larger than expected and this discrepancy is probably due to some limitations of our model.

DOI: 10.1103/PhysRevA.88.043628 PACS number(s): 37.25.+k, 03.75.Dg, 03.65.Vf

I. INTRODUCTION

The topological He-McKellar-Wilkens (HMW) phase introduced in 1993 by He and McKellar [1] and in 1994 by Wilkens [2] has not been tested since its theoretical discovery. We have recently published such a test [3] using our lithium atom interferometer. In the preceding paper [4] quoted here as HMWI, we have recalled the theory of this topological phase and its relations with the Aharonov-Bohm [5] and Aharonov-Casher phases [6]. We have also discussed the effects of phase dispersion on interferometer signals and we have considered in detail the phase shifts induced by electric and magnetic fields, namely, the dynamical phase shifts due to the Stark and Zeeman Hamiltonians and the topological phase shift due to the Aharonov-Casher effect. The present paper is devoted to a detailed presentation of the experiment, of its results, and of the analysis of the stray effects which have complicated the test of the HMW phase.

In the following sections, we first describe the experiment, the data recording procedure, and the interferometer signals (Sec. II). Then we discuss the effects of the electric fields (Sec. III) and of the magnetic fields (Sec. IV). Section V presents the data set for the HMW phase measurement and the raw results. The model describing the stray effects due to phase shift dispersion, introduced in HMWI and developed in the Appendix, is tested thanks to numerous and sensitive measurements of the fringe phase and visibility (Sec. VI). Because of this model, we have been able to reject most of the stray effects and to measure the HMW phase, as detailed in Sec. VII. A conclusion (Sec. VIII) summarizes what we have learnt from this experiment, recalls the open questions (in particular a phase shift presently not understood), and discusses how to improve this experiment.

II. THE EXPERIMENT: THE SETUP AND THE DATA RECORDING PROCEDURE

In this part, we briefly describe our atom interferometer and, with greater detail, the interaction region used to observe the HMW effect. We also describe the compensator coil used to produce a magnetic field gradient opposite to the one due to the HMW interaction region. Finally, we explain our data recording procedure which rejects the interferometer phase drifts.

A. Our atom interferometer

Our separated-arm atom interferometer (see Fig. 1) has been previously described [7–9]. Here, we present only its main features and some recent improvements. The atomic source is a supersonic beam of lithium seeded in argon, with a mean velocity $v_m \approx 1065$ m/s. Once collimated by two 18-μm-wide slits, this beam has a transverse velocity distribution with a width comparable to the recoil velocity of lithium, $v_r \approx 9$ cm/s. This beam is then diffracted by three quasiresonant laser standing waves in the Bragg regime: the present experiment uses first-order diffraction, with only two diffracted beams of orders 0 and +1 (or −1). We thus get a Mach-Zehnder atom interferometer with two output beams carrying complementary interference signals. One output beam is selected by a slit and its intensity I, measured by a surface ionization detector, is given by

$$I = I_0[1 + \mathcal{V}\cos(\varphi_d + \varphi_p)]. \quad (1)$$

I_0 is the mean intensity and $\mathcal{V}$ the fringe visibility. The phase is the sum of the phase φ_p due to perturbations and the phase φ_d due to the diffraction process: $\varphi_d = 2k_L(x_1 - 2x_2 + x_3)$, where k_L is the laser wave vector and x_i the x position of mirror M_i. The choice of the laser frequency, at about 2 GHz on the blue side of the $^2S_{1/2}$-$^2P_{3/2}$ transition of ^{7}Li, and the 92.5% natural abundance of ^{7}Li ensure that the interferometer signal is almost purely due to this isotope [7,10]. To record interference fringes, we sweep the phase φ_d by varying x_3 with a piezoelectric actuator. We measure the variations of x_3 with a Michelson interferometer [9]. Intense signals, with a mean

*jacques.vigue@irsamc.ups-tlse.fr

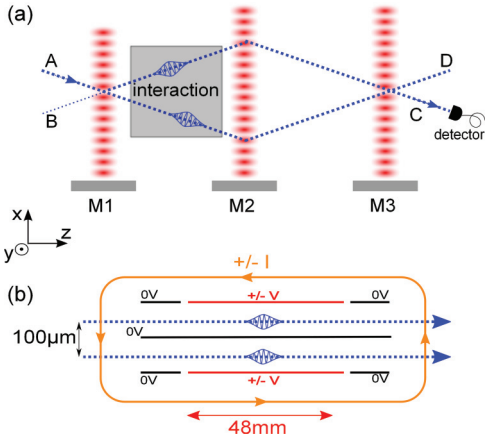

FIG. 1. (Color online) Schematic top views (not to scale) of our atom interferometer (a) and the interaction region for the observation of the HMW phase (b). Our atom interferometer is a Mach-Zehnder interferometer, with two entrances A and B (only A is used) and two exits C and D (C is detected). An atomic beam (dotted blue lines) entering by A is diffracted by three quasiresonant laser standing waves produced by the mirrors M_i. The largest distance between interferometer arms, about 100 μm, occurs just before the second laser standing wave, where we introduce the interaction region. The opposite electric fields necessary for the observation of the HMW phase are horizontal. They are produced by two plane capacitors (high-voltage electrodes in red; grounded electrodes in black). The septum is a thin common electrode located between the two interferometer arms represented by dotted blue lines. Two rectangular coils (represented by the orange rectangle) produce the vertical magnetic field.

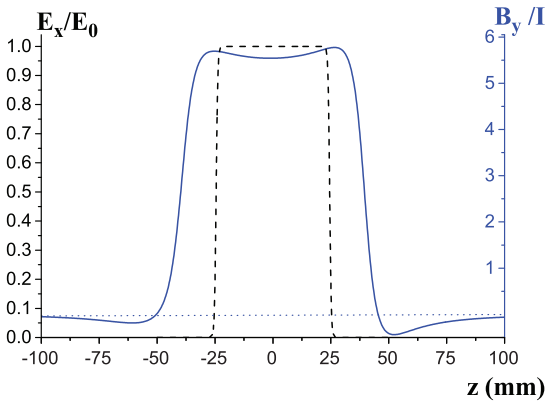

FIG. 2. (Color online) Calculated components E_x (dashed line) and B_y (full line) as a function of z in the interaction region. For the electric field, the plotted quantity is E_x/E_0, where $E_0 = V/h$ is the field of an infinite plane capacitor, with a spacing h and an applied voltage V. For the magnetic field, the plotted quantity B_y/I, where I is the coil current, is in units of 10^{-4} T/A.

intensity $I_0 \approx 60\,000$ atoms/s and a high fringe visibility $\mathcal{V} \approx 70\%$ provide a large phase sensitivity, with a value $\Delta\varphi_{\min} \approx 25$ mrad/$\sqrt{\text{Hz}}$ achieved in practice.

B. The HMW interaction region

A HMW phase is induced when an atom propagates in crossed electric and magnetic fields, both transverse to the atom velocity. Our experimental arrangement is inspired by the ideas of Wei *et al.* [11], the electric fields are horizontal, in the interferometer plane, and opposite on the two interferometer arms, while the common magnetic field is vertical and as homogeneous as possible.

The electric fields are produced by a double capacitor with a septum [12] located between the interferometer arms (see Fig. 1). Each of the two capacitors is similar to the one we used for the measurement of the electric polarizability of lithium [13]. The outer electrodes are made of polished 5-mm-thick glass plates with evaporated aluminum electrodes. A central high-voltage electrode of length $2a \approx 48$ mm is separated from two 5-mm-long grounded guard electrodes by 1-mm-wide gaps: these gaps withstand a voltage larger than 1 kV. The septum is a 30-μm-thick aluminum foil. The capacitors are assembled by gluing together the electrodes and the glass spacers (thickness $h \approx 1.10$ mm) with Epotex 301 glue (Epoxy Technologies). The septum must remain well stretched, even if the capacitor temperature varies. We have acquired the ability to glue a prestretched septum on the electrode-spacer assembly heated near 65 °C and, due to differential thermal expansion, the septum is fully stretched when the assembly has cooled down [14]. The capacitors are as symmetric as possible and they are powered by slightly different voltages issuing from the same power supply, with an adjustable voltage ratio thanks to potentiometers. This arrangement minimizes Stark phase noise due to voltage fluctuations of the power supply. Figure 2 presents the calculated z variation of the electric field E_x component, which is relevant for the HMW phase. E_x is calculated at the septum surface whereas the atom-septum mean distance is near 40 μm, but the associated correction is very small [13].

The capacitor assembly is inserted in a brass support on which we have coiled 1.5-mm-diameter enameled copper wires to produce the vertical magnetic field needed for the HMW phase. We use two rectangular coils, located below and above the interferometer plane, each coil being made of two layers and each layer of seven windings, glued together and to the brass support with a high-thermal-conductivity glue (Stycast 2850 FT). A 2-mm-internal-diameter copper pipe is also glued on the brass support at mid-distance between the two coils and with a 6 cm^3/s flow of tap water (a low flow rate chosen to minimize vibrations), the temperature rise is about 0.5 K/W. Usually, we apply a current I in the coils 50% of the time so that the maximum current $I = 25$ A induces a 20 W mean Joule power and a temperature rise near 10 K. In Fig. 2, we have plotted the calculated z variation of the magnetic field B_y component which is the one relevant for the HMW phase. As discussed in HMWI, a Zeeman phase shift appears if the magnetic field modulus B is different on the two interferometer arms, and we have minimized this difference by careful coiling and design of the geometry of the connection wires.

The HMW interaction region is placed just ahead of the second laser standing wave, where the distance between the center of the interferometer arms is largest, close to 100 μm. In order not to induce vibrations of the standing-wave mirrors, the interaction region is suspended from the top of the vacuum chamber. Initial adjustments of the rotation around the horizontal z axis and the vertical y axis are performed

with optical methods. Rotation around the y axis as well as translation in the x direction can be operated under vacuum, and the ultimate tunings are done with the atom interferometer running. After optimization of the interferometer signal, the mean intensity I_0 and the fringe visibility $\mathcal{V}$ are not modified by the presence of the septum between the two arms.

The magnetic field produced by the HMW coil was measured with a three-dimensional Hall probe and compared to the field calculations, showing a good agreement. Concerning the electric field, calibration measurements using the atom interferometer (described in Sec. III A) yield an accurate knowledge of each capacitor geometry needed for electric field calculations. With the electric and magnetic field components E_x and B_y as functions of z, we can calculate the integral $\int E_x B_y dz$ and thanks to the very accurate knowledge of the electric polarizability of the lithium atom [13,16], we can predict the slope of the HMW phase as a function of the product VI:

$$\varphi_{\mathrm{HMW}}(V,I)/(VI) = -(1.28 \pm 0.03) \times 10^{-6}\ \mathrm{rad/V\,A}, \qquad (2)$$

where the error bar is due to the uncertainty on the geometrical parameters of the capacitors and of the HMW coil.

C. Compensator coil

In spite of our efforts, the magnetic field of the HMW coil is slightly different on the two interferometer arms, with a mean relative difference $|\Delta B|/B \approx 10^{-4}$. This difference is most probably due to a bad centering of the septum in the HMW coil, with a distance between the coil symmetry plane and the septum of the order of 250 μm. For $I = 25$ A, the induced Zeeman phase shift is equal to $\varphi_Z(F,m_F) \approx \pm 11$ rad for the $F = 2, m_F = \pm 2$ sublevels. We compensate these phase shifts using a supplementary coil producing an opposite magnetic field gradient along the x axis. This so-called compensator coil is made of nine turns of copper wire on a 30-mm-diameter aluminum cylinder. It is located at mid-distance between the first and second laser standing waves, with a mean distance between the compensator coil and the interferometer arms near 10 mm. This coil is cooled by conduction through its support and the temperature rise limits its current I_C to 5 A, if applied only 50% of the time. Then the magnetic field experienced by the atoms is below 2×10^{-3} T, a range for which the Zeeman effect is linear.

D. Data recording and signals

In our previous experiments [9,10,13,17], we deduced the effect of a perturbation by comparing fringe signals successively recorded with and without this perturbation. The phase measured in the absence of perturbation, which should be constant, drifts with time, typically by several tens of milliradians over the few minutes needed for recording a high-quality fringe signal. These drifts are not linear in time and they are due to minute distortions of the rail supporting the standing-wave mirrors. Their magnitude is due to the high sensitivity of the diffraction phase φ_d to the mirror positions, with $d\varphi_d/dx_i \approx +20$ rad/μm for M_1 or M_3 and -40 rad/μm for M_2. They were the main limitation of our phase-shift measurements. For the present experiment, we have almost canceled the sensitivity to these drifts by applying

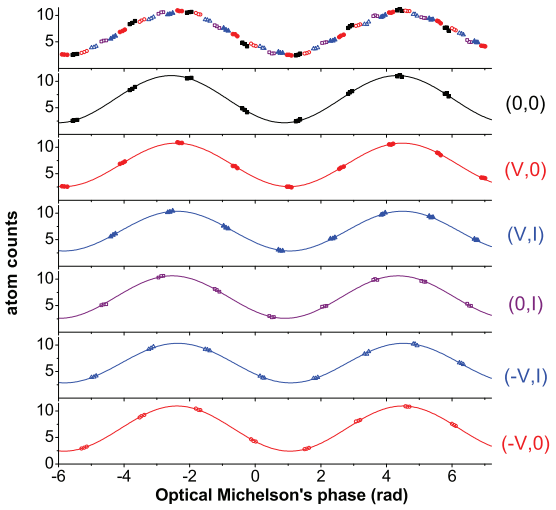

FIG. 3. (Color online) Recorded data with six (V,I) configurations during a single fringe scan: the number of detected atoms per second (the unit is 10^4 detected atoms/s and the counting period is 0.1 s) is plotted as a function of the phase of the optical Michelson interferometer which directly maps the position x_3 of mirror M_3. The signals corresponding to different field configurations are plotted with different symbols: black squares for $(0,0)$, red bullets for $(V,0)$, blue full triangles for (V,I), open violet squares for $(0,I)$, open blue triangles for $(-V,I)$, and open red circles for $(-V,0)$. The top graph represents the signal as it is recorded and the signal corresponding to each one of the six (V,I) configurations is plotted separately below with its best fit.

several field configurations during each fringe recording: a field configuration is defined by the (V,I) values, where V is the capacitor mean voltage and I the current in the HMW coil (this current is accompanied by a current I_C in the compensator coil, as explained below). We have used either four configurations $(0,0)$, $(V,0)$, (V,I), and $(0,I)$ or six configurations, by adding $(-V,I)$ and $(-V,0)$ to this list. A typical fringe recording with six configurations is shown in Fig. 3. A fit of the different fringe signal systems is made using Eq. (1), where the fringe systems of all configurations share the same value of the diffraction phase φ_d. We thus get the mean intensity $I_0(V,I)$, the fringe phase $\varphi(V,I)$, and the fringe visibility $\mathcal{V}(V,I)$ for each field configuration. In this way, we deduce the effects of the application of the electromagnetic field corresponding to each configuration. I_0 is independent of the field configuration, but the visibility and the phase are both modified. We define a relative visibility and a fringe phase shift for each field configuration by

$$\begin{aligned}
\mathcal{V}_E(V) &= \mathcal{V}(V,0)/\mathcal{V}(0,0),\\
\varphi_E(V) &= \varphi(V,0) - \varphi(0,0),\\
\mathcal{V}_B(I) &= \mathcal{V}(0,I)/\mathcal{V}(0,0),\\
\varphi_B(I) &= \varphi(0,I) - \varphi(0,0),\\
\mathcal{V}_{EB}(V,I) &= \frac{\mathcal{V}_{E+B}(V,I)}{\mathcal{V}_E(V)\mathcal{V}_B(I)} = \frac{\mathcal{V}(V,I)\mathcal{V}(0,0)}{\mathcal{V}(V,0)\mathcal{V}(0,I)},\\
\varphi_{EB}(V,I) &= \varphi_{E+B}(V,I) - \varphi_E(V) - \varphi_B(I)\\
&= \varphi(V,I) - \varphi(V,0) - \varphi(0,I) + \varphi(0,0).
\end{aligned} \qquad (3)$$

$\mathcal{V}_E(V)$ and $\varphi_E(V)$ are the fringe relative visibility and phase shift with the electric field only; $\mathcal{V}_B(I)$ and $\varphi_B(I)$ are the fringe relative visibility and phase shift with the magnetic field only; and $\mathcal{V}_{E+B}(V,I)$ and $\varphi_{E+B}(V,I)$ are the fringe relative visibility and phase shift with the electric and magnetic fields applied simultaneously. A fringe scan such as shown in Fig. 3 lasts about 20 s, a duration sufficiently small to ensure quasilinearity of the interferometer phase drift with time [an exactly linear phase drift alters only φ_d and leaves the results of Eqs. (3) unchanged]. The error bars are about 2% on the relative visibility and 30 mrad on the induced phase shifts. We repeat about 100 successive fringe scans, taking care that the fringe scan period and the field configuration period are not commensurate, in order to avoid any possible bias in the fits. The error bars on the averages of such a scan series are near 0.2% for the relative visibility and near 3 mrad for the phase shifts, small enough to detect fine perturbations of the interference fringe signals and to understand systematic effects.

III. EFFECTS OF THE ELECTRIC FIELDS ON THE FRINGE PHASE AND VISIBILITY

A. Experimental study of polarizability phase shifts

During calibration measurements, we applied a voltage V to one capacitor only, the other one being grounded. Figure 4 presents typical results for the fringe visibility $\mathcal{V}_r = \mathcal{V}(V)/\mathcal{V}(0)$ and the induced phase shift $\varphi_S(V)$ as a function of V^2. These measurements were fitted using Eqs. (19), (20), and (31) of HMWI, which yields the value of the parallel speed ratio $S_\parallel = 9.25 \pm 0.08$ and the values of the Stark phase shifts induced by each capacitor for the mean atom velocity: $\varphi_u/V^2 = (-4.830 \pm 0.005)$ rad/V^2 and $\varphi_l/V^2 = (4.760 \pm 0.007)$ rad/V^2. Using the very accurate theoretical value [16] of the lithium atom electric polarizability α, we may deduce the geometrical parameter $L_{\rm eff}/h^2$ for both capacitors ($L_{\rm eff}$ is the capacitor effective length and h the plate spacing [13]). The effective length is the same for both capacitors with a good accuracy, $L_{\rm eff} \approx 48 \pm 0.5$ mm, so that these experiments provide measurements of the mean values of the

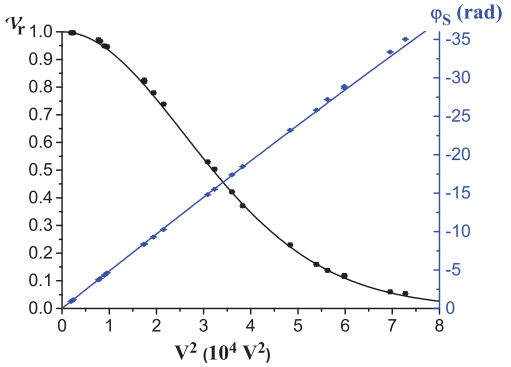

FIG. 4. (Color online) The relative visibility $\mathcal{V}_r$ (left scale, black squares and line) and the fringe phase shift φ_S (rad) (right scale, blue bullets and line) are plotted as a function of V^2, where V is the voltage applied to one capacitor only. The points are experimental and the curves are their best fits.

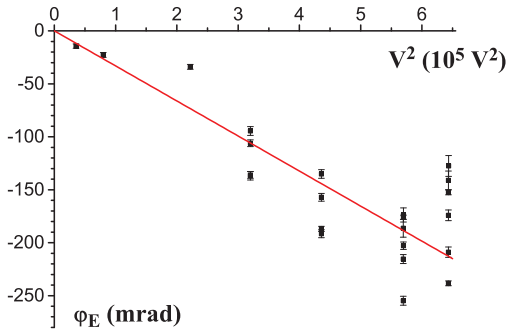

FIG. 5. (Color online) Fringe phase shifts induced by electric fields applied to both capacitors: the measured phase shift $\varphi_E(V)$ is plotted as a function of V^2 where V is the mean of the voltages V_u and V_l applied to the two capacitors. The points are experimental and the straight line is the best fit.

capacitor spacings $h_u = 1.101 \pm 0.006$ mm and $h_l = 1.109 \pm 0.006$ mm.

B. Experiments with both electric fields on: Phase measurements

When we apply electric fields to both capacitors, with the voltage ratio tuned to cancel the Stark phase shift $\varphi_E(V)$, we observe a residual phase shift due to imperfect tuning: $\varphi_E(V)$ is small and approximately proportional to V^2, but with large fluctuations of the measured value (see Fig. 5). We have observed that $\varphi_E(V)$ drifts with time when the interaction region temperature varies: this behavior can be explained by a delay of the expansion of one capacitor with respect to the other one, a delay due to the low thermal conductivity of glass. For $V = 800$ V, the Stark phase induced on each interferometer arm can reach $\varphi_{S,u} \approx \varphi_{S,l} \approx 307$ rad. Then a typical deviation for $\varphi_E(V)$ of 0.05 rad from its mean value corresponds to a 1.7×10^{-4} relative variation of the geometrical parameter $L_{\rm eff}/h^2$ of one capacitor with respect to the other one. This variation is somewhat larger than expected for a simple thermal expansion effect with a temperature variation smaller than 10 K. The conclusion is that, because of dispersion and drift, the residual Stark phase shift $\varphi_E(V)$ does not carry much useful information.

In the experiments with six field configurations, we can measure the difference of the Stark phase shifts for opposite V values, with an error bar close to 1 mrad. Figure 6 plots the quantity $[\varphi_E(|V|) - \varphi_E(-|V|)]/2$ as a function of $|V|$. Equation (B4) of HMWI predicts that the only V-odd term in $\langle\varphi_S\rangle$ is the contact potential phase $\langle\varphi_{Sc}\rangle$ so that

$$[\varphi_E(|V|) - \varphi_E(-|V|)]/2 = 2\varphi_0 \frac{\langle\bar{V}_{c,u}\rangle - \langle\bar{V}_{c,l}\rangle}{V}. \quad (4)$$

We have fitted the measured values of $[\varphi_E(|V|) - \varphi_E(-|V|)]/2$ by a function $a + b|V|$. The fitted a value, $a = 10 \pm 1$ mrad, is not explained by Eq. (4) but its presence might be due to the use of different power supplies, one per polarity, to produce opposite voltages. The fitted slope $b = (-6 \pm 2) \times 10^{-3}$ mrad/V can be explained by a difference of the mean contact potentials $(\langle\bar{V}_{c,u}\rangle - \langle\bar{V}_{c,l}\rangle) = 6 \pm 2$ mV: we may conclude that contact potentials play a very minor role

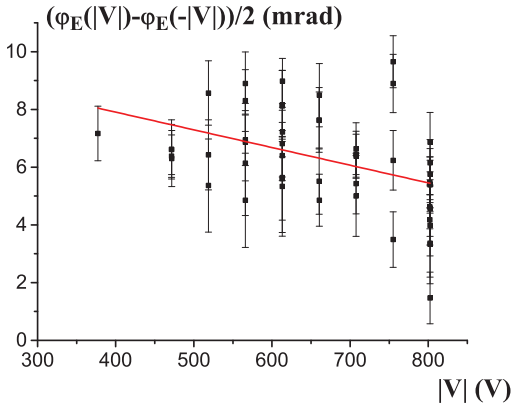

FIG. 6. (Color online) Fringe phase shifts induced by electric fields applied to both capacitors: the difference quantity $[\varphi_E(|V|) - \varphi_E(-|V|)]/2$ is plotted as a function of $|V|$. The points are experimental and the straight line is the best linear fit.

in our experiment and this idea will be supported by further results.

C. Experiments with both electric fields on: Visibility measurements

We now discuss the measurements of the relative visibility $\mathcal{V}_E(V)$. The residual Stark phase shift φ_E is sufficiently small to neglect any effect of the velocity dispersion on the visibility. The relative visibility was highly dependent on the standing-wave mirrors' alignment. Therefore the collected data for $\mathcal{V}_E(V)$ were partitioned into seven different sets: within a given set, this interferometer alignment is identical for all the data points. Fig. 7 presents two of these data sets. All the sets exhibit different behaviors, but are well independently fitted using the following equation:

$$\mathcal{V}_E(V) = 1 - \sum_{i=1,4} k_{Vi} V^i. \tag{5}$$

As illustrated by Fig. 7, the relative visibility can become larger than 1, a result apparently surprising. This happens when phase dispersions which exist when no interaction is applied are partially canceled by the phase dispersion due to

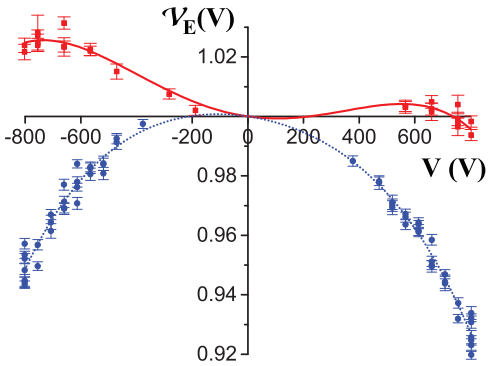

FIG. 7. (Color online) Fringe relative visibility $\mathcal{V}_E(V)$ as a function of the applied mean voltage V: the points are experimental, with different symbols (red squares and blue bullets) for two different alignments of the atom interferometer. The data points are fitted by Eq. (5) (red full line and blue dotted line).

the application of the electric fields. The preexisting phase dispersions originate from the Zeeman phase shifts due to the inhomogeneity of the laboratory magnetic field when $I = I_C = 0$ and from the diffraction phase which presents a spatial dispersion because of an imperfect alignment of the laser standing-wave mirrors M_i. The application of the electric fields induces an Aharonov-Casher phase shift and a Stark phase shift: the Aharonov-Casher phase shift is dispersed because of its dependence on the F,m_F sublevel, and the Stark phase shift is dispersed because of capacitor defects. We must describe all these effects, in order to explain the behavior of $\mathcal{V}_E(V)$. Assuming a balanced hyperfine population, i.e., $\chi = 0$ (χ is defined in Appendix A of HMWI), we use Eqs. (23), (42), (46), and (47) of HMWI to evaluate $\mathcal{V}(0,0)$:

$$\frac{\mathcal{V}(0,0)}{\mathcal{V}_0} = \left[1 - \frac{\langle(\delta\varphi_d)^2\rangle}{2}\right]\frac{\mathcal{V}_{B0}}{\mathcal{V}_0} \quad \text{with} \quad \frac{\mathcal{V}_{B0}}{\mathcal{V}_0} = \frac{1 + \cos(J_0) + 2\cos(J_0/2)}{4}. \tag{6}$$

$\delta\varphi_d(y)$ is the dispersion of the diffraction phase and $\mathcal{V}_{B0}$ is the visibility modified by the inhomogeneity of the laboratory magnetic field. Because of these two effects, the observed visibility $\mathcal{V}(0,0)$ is smaller than its optimum value $\mathcal{V}_0$. With electric fields on both arms, the Stark phase shift $\varphi_S(y)$ is a function of y, and the Aharonov-Casher phase shift $\varphi_{AC}(F,m_F)$ is given by $\varphi_{AC}(2,m_F) = -\varphi_{AC}(1,m_F) = (m_F/2)\varphi_{AC}(2,2)$ (this formula is valid because the Zeeman effect is linear in the laboratory field). Using Eqs. (A9), (A15), and (A16), we deduce the fringe visibility $\mathcal{V}(V,0)$:

$$\frac{\mathcal{V}(V,0)}{\mathcal{V}_0} = \mathcal{V}_{B0}\left[1 - \frac{\langle(\delta\varphi_d + \delta\varphi_S)^2\rangle}{2}\right] - \frac{\varphi_{AC}(2,2)}{4}\left[\sin(J_0) + \sin\left(\frac{J_0}{2}\right)\right]. \tag{7}$$

The last term of the right-hand side is a first-order Taylor expansion of the trigonometric functions of φ_{AC}, valid because $|\varphi_{AC}| \leqslant 70$ mrad in the present experiment. We get the relative visibility $\mathcal{V}_E(V) = \mathcal{V}(V,0)/\mathcal{V}(0,0)$:

$$\mathcal{V}_E(V) = 1 - \frac{\langle(\delta\varphi_S)^2 + 2\delta\varphi_d\delta\varphi_S\rangle}{2} - \frac{\varphi_{AC}(2,2)}{4\mathcal{V}_{B0}}\left[\sin(J_0) + \sin\left(\frac{J_0}{2}\right)\right]. \tag{8}$$

The dispersion $\delta\varphi_S$ of the Stark phase shift is given by $\delta\varphi_S = \delta\varphi_{S,g} + \delta\varphi_{S,c}$ with the geometrical defect term $\delta\varphi_{S,g} \propto V^2$ and the contact potential term $\delta\varphi_{S,c} \propto V$. $\varphi_{AC}(2,2) \propto V$ while $\delta\varphi_d$ and J_0 are independent of V. We thus deduce the values of the k_{Vi} coefficients:

$$\begin{aligned} k_{V1} &= \langle\delta\varphi_d\delta\varphi_{S,c}\rangle + \frac{\varphi_{AC}(2,2)}{4\mathcal{V}_{B0}}\left[\sin(J_0) + \sin\left(\frac{J_0}{2}\right)\right], \\ k_{V2} &= \langle(\delta\varphi_{S,c})^2/2\rangle + \langle\delta\varphi_d\delta\varphi_{S,g}\rangle, \\ k_{V3} &= \langle\delta\varphi_{S,g}\delta\varphi_{S,c}\rangle, \\ k_{V4} &= \langle(\delta\varphi_{S,g})^2/2\rangle. \end{aligned} \tag{9}$$

Discussed below is a comparison of Eqs. (9) with the results of fits of $\mathcal{V}_E(V)$ for the seven available data sets: at the same time, we test the validity of our description of experimental

defects and we get some insights into the nature of the systematic effects. All k_{V4} values are positive and compatible with their mean, $k_{V4} = (6.0 \pm 0.5) \times 10^{-14}$ V^{-4}. This is in agreement with Eqs. (9) which predicts that k_{V4} is positive and depends solely on the geometrical defects of the capacitors and not of the interferometer alignment. From this result, we may estimate the geometrical defects of the capacitors if we assume that the spacing difference $\Delta h = h_u - h_l$ is the main defect and that it varies linearly with y. We then find that Δh varies by about 1.4 μm over the y range sampled by the atoms (about 2 mm). This Δh value appears to be quite small for capacitors assembled by gluing parts together but, when $V = 800$ V, this small defect is sufficient to induce a total dispersion of the Stark phase shift along the atomic beam height equal to 0.8 rad.

All k_{V3} values (excepted one) are compatible with 0, with a very small mean value $k_{V3} = (0.04 \pm 1.7) \times 10^{-12}$ V^{-3}, corresponding to $\langle \delta\varphi_{S,g} \delta\varphi_{S,c} \rangle < 10^{-6}$ rad^2 for $V = 800$ V. The dispersions $\delta\varphi_{S,g}$ and $\delta\varphi_{S,c}$ are not correlated, in agreement with the idea that contact potentials fluctuate on small scales and that geometrical defects are smooth functions of y.

Each k_{V2} value has a small error bar but k_{V2} varies strongly from one set of data to the next, covering the range from -5×10^{-8} to $+13 \times 10^{-8}$ V^{-2}. These large variations prove that the dominant contribution comes from the interferometer alignment, i.e., from the $\langle \delta\varphi_d \delta\varphi_{S,g} \rangle$ term. When $\delta\varphi_d$ and $\delta\varphi_{S,g}$ have opposite variations, the electric fields increase the visibility, as observed in Fig. 7.

All k_{V1} values are compatible with their mean $k_{V1} = (1.40 \pm 0.07) \times 10^{-5}$ V^{-1}. The first term $\langle \delta\varphi_d \delta\varphi_{S,c} \rangle$, which involves the contact potential term, is expected to be very small for the same reasons which explain the weakness of k_{V3} and, if this term is not negligible, k_{V1} should vary with the interferometer alignment like k_{V2}. The second term, which is due to the Aharonov-Casher phase shift in the laboratory magnetic field, must be dominant. Assuming that the laboratory magnetic field $\mathbf{B}_0$ is constant over the capacitor length and that the electric fields are equal to $E_0 = V/h$ over a length $L_{\text{eff}} \approx 48$ mm, we estimate the Aharonov-Casher phase shift given in Eqs. (2) and (49) of HMWI:

$$\varphi_{AC}(2,2) = \frac{2\mu_B E_0 L_{\text{eff}}}{\hbar c^2} \mathbf{y} \cdot \mathbf{u}_0, \tag{10}$$

where $\mathbf{u}_0 = \mathbf{B}_0/B_0$ points in the direction of $\mathbf{B}_0$. The measurements presented in the next section give access to $J_0 \approx -0.61$ rad and to $\mathcal{V}_{B0} \approx 0.93$. We thus deduce $\mathbf{y} \cdot \mathbf{u}_0 \approx -0.7$, i.e., $\mathbf{B}_0$ points downward, at about 45° from the vertical, in agreement with direct measurements of the local laboratory field.

IV. EFFECTS OF THE MAGNETIC FIELD ON THE FRINGE PHASE AND VISIBILITY

A. Experiments with the compensator coil only

We have measured the relative visibility $\mathcal{V}_B(I_C)$ and the phase shift $\varphi_B(I_C)$ of the interference fringes as a function of the compensator coil current I_C. The results are plotted in Fig. 8 with fits based on Eqs. (42) and (45) of HMWI, with $J_1 = A_{J1,C}|I_C - I_{0,C}| + J_{0,C}$ and assuming balanced sublevel populations (see Appendix A of HMWI).

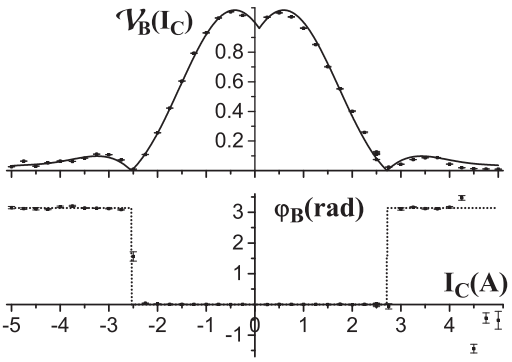

FIG. 8. Relative visibility (upper panel) and phase shift (lower panel) as functions of the compensator current I_C (A). The points are experimental and the curves represent their best fit, with $A_{J1,C} = 1.52 \pm 0.02$ rad/A, $I_{0,C} = 0.09 \pm 0.02$ A, and $J_{0,C} = -0.63 \pm 0.03$ rad. The minor deviations which appear when $I_C > 4$ A are probably due to the arbitrary assumption of balanced sublevel populations ($\chi = 0$) for this particular example.

B. Experiments with the HMW coil only

The relative visibility $\mathcal{V}_B(I)$ and the phase shift $\varphi_B(I)$ were measured as functions of the HMW coil current I. Some of the results are plotted in Fig. 9. Equation (41) of HMWI gives $\varphi_Z(F,m_F)$ as a function of J_1, J_2, and J_3, and we use $J_1 = A_{J1}|I - I_0| + J_{0,I}$, $J_2 = A_{J2} I^2$, and $J_3 = A_{J3}|I|^3$ to fit the data. The hyperfine population imbalance parameter χ is also fitted, with a different value for each data set corresponding to a slightly different laser frequency.

C. Experiments with both coils and global fit

With a HMW coil current I and a compensator coil current I_C, optimum compensation of the linear part of the Zeeman phase shift is obtained with $I_C \approx |I|/3$. When $|I| > 15$ A, it is impossible to use $I_C > 5$ because the compensator coil

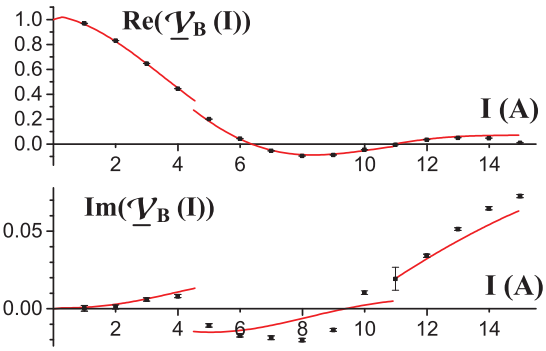

FIG. 9. (Color online) Real and imaginary parts of the complex fringe visibility as functions of the HMW coil current I [note the expanded scale for Im($\mathcal{V}_B(I)$)]. The points are experimental and the curves are the results of best fits, with three different χ values: $\chi = 0.077$ for $I = 0$–4 A; $\chi = -0.014$ for $I = 5$–10 A; $\chi = -0.062$ for $I = 11$–15 A. When these experiments were done, we had not understood that the laser frequency must be tightly controlled in order to keep χ very small and this explains why large χ values are observed. We get $A_{J1} = -0.46 \pm 0.02$ rad/A, $A_{J2} = (-110 \pm 8) \times 10^{-4}$ rad/A^2, $A_{J3} = (-20 \pm 4) \times 10^{-5}$ rad/A^3, $I_0 = 0.32 \pm 0.05$ A, and $J_{0,I} = -0.55 \pm 0.13$ rad.

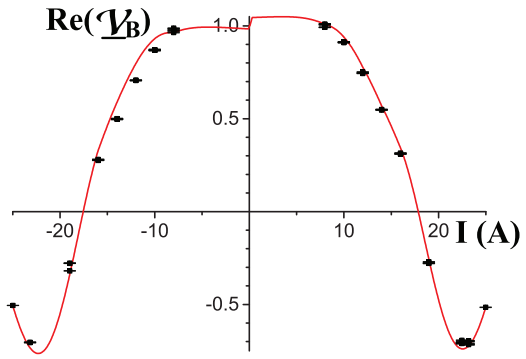

FIG. 10. (Color online) Real part of the complex relative visibility $\mathrm{Re}\left(\underline{\mathcal{V}}_B\right)(I)$ plotted as a function of the HMW current I, the compensator current I_C having the value described in the text. The points are experimental and the curve is calculated using the global fit results, Eqs. (11), with the population imbalance parameter fixed at $\chi = 0$. We have not represented the imaginary part $\mathrm{Im}(\underline{\mathcal{V}}_B)(I)$ which is very small (<0.03) and very sensitive to χ.

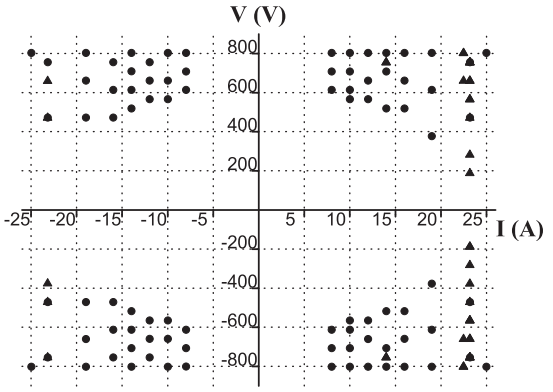

FIG. 11. Data set collected for the measurement of the HMW phase. Each run is represented in the I,V plane by a triangle (a bullet) for a four-field (six-field) experiment.

temperature rises too much and, thus, we have used $I_C = 5$ A. Figure 10 presents the relative visibility $\mathcal{V}_B$ as a function of I. Comparison with Fig. 9 proves the efficiency of the compensator: when $I_C = 0$, $\mathcal{V}_B(I)$ vanishes for $I \approx 6$ A while, with the compensator in operation, it remains larger than 80% if $|I| \leqslant 12$ A and vanishes only for $|I| \approx 18$ A. The revival observed for $I = 23$ A, with a relative visibility near -70% and a phase shift close to π, is explained in Ref. [15].

In order to have the best estimate of the Zeeman phase shifts induced during the HMW effect measurements, we performed a single global fit of all the data recorded while testing the effects of magnetic fields. This data set was collected during the HMW effect measurements using both coils (with I_C related to I for optimum compensation) as well as during calibration measurements using either both coils (with different relative tuning of I and I_C) or only one coil. As introduced in HMWI, the Zeeman phase shifts are calculated using $J_1 = A_{J1}|I - I_0| + A_{J1,C}|I_C - I_{0,C}| + J_{0,I+C}$, with $J_{0,I+C} = J_0 - A_{J1}|I_0| - A_{J1,C}|I_{0,C}|$. The data set for $\mathcal{V}_B\,(I, I_C)$ and $\varphi_B\,(I, I_C)$ includes about 150 data points which belong to 31 series corresponding to slightly different laser frequencies, and a different χ value is fitted for each series. Here are the fitted values of J_0, I_0, A_{Ji}, $I_{0,C}$, and $A_{J1,C}$ provided by this global fit:

$$\begin{aligned} J_0 &= -0.61 \pm 0.01 \text{ rad}, \\ I_0 &= 0.31 \pm 0.03 \text{ A}, \\ A_{J1} &= -0.430 \pm 0.005 \text{ rad/A}, \\ A_{J2} &= (-662 \pm 5) \times 10^{-5} \text{ rad/A}^2, \\ A_{J3} &= (-180 \pm 5) \times 10^{-6} \text{ rad/A}^3, \\ I_{0,C} &= (22 \pm 9) \times 10^{-3} \text{ A}, \\ A_{J1,C} &= 1.43 \pm 0.015 \text{ rad/A}. \end{aligned} \tag{11}$$

V. DATA SET FOR THE HMW PHASE MEASUREMENT AND RAW RESULTS

Figure 11 presents the data set collected for the HMW phase measurement. As φ_{HMW} is very small and proportional to the product VI, we have chosen to record data with large values either of V or of I, so that we have no data point near the origin.

The measured values of the phase shift $\varphi_{EB}(V, I)$ are plotted as a function of the product VI in Fig. 12: these results do not agree with the predicted variations of φ_{HMW} and we explain this discrepancy by stray phase shifts which appear when the electric and magnetic fields are simultaneously applied. The origins of these stray phases have been explained on general grounds in HMWI and the detailed calculation is presented in the Appendix of the present paper. We are going to test these calculations first on the relative visibility $\mathcal{V}_{EB}(V, I)$ and afterward on the phase shift $\varphi_{EB}(V, I)$. The various stray effects differ by their symmetry with respect to the reversal of the electric and/or magnetic fields and, in order to test these effects separately, it is necessary to extract the even and odd parts of these quantities with respect to field reversals by combining measurements for opposite V or I values. For any quantity $f(V, I)$, the mean $\mathcal{M}_X f(V, I)$ and the half difference $\Delta_X f(V, I)$ for opposite values of V (then $X = E$) or of I (then

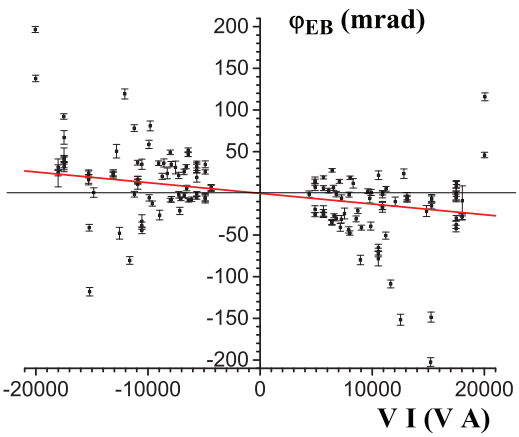

FIG. 12. (Color online) Measured values of $\varphi_{EB}(V, I)$ given by Eq. (3) as a function of the VI product measured in V A. The (red) full line represents the expected value of the HMW phase, $\varphi_{\mathrm{HMW}}(V, I) = -(1.28 \pm 0.03) \times 10^{-6} VI$ rad.

$X = B$) are equal to

$$\begin{aligned} \mathcal{M}_E f(V,I) &= [f(V,I) + f(-V,I)]/2, \\ \Delta_E f(V,I) &= [f(V,I) - f(-V,I)]/2, \\ \mathcal{M}_B f(V,I) &= [f(V,I) + f(V,-I)]/2, \\ \Delta_B f(V,I) &= [f(V,I) - f(V,-I)]/2. \end{aligned} \tag{12}$$

Most experiments were done with six field configurations and they provide simultaneous measurements of $\mathcal{V}_{EB}(V,I)$ and $\varphi_{EB}(V,I)$ for opposite voltages, with exactly the same current I and the same value of the population imbalance parameter χ: we thus have very sensitive tests of the effects of electric field reversal.

VI. SOME EXPERIMENTAL TESTS OF THE EFFECTS OF STRAY PHASES

We are going to test the predictions of the calculations described in the Appendix of the present paper.

A. Tests involving the fringe visibility

Following Eq. (A13), four combinations of $\mathcal{V}_{EV}(V,I)$ separate the contributions of the four $D_{\pm,\pm}(V,I)$ terms. However, as shown by Eq. (A18), the quantity $\mathcal{V}_{EB}$ also includes a contribution due to the Aharonov-Casher effect in the corresponding $(V,0)$ field configuration. It is given by the term $D_{\mathrm{AC},B0}(V)/D_{0,B0}$, with a value close to 1.1% for $V =$ 800 V. Because it involves the AC phase, this effect is an odd function of the voltage V. We eliminate this contribution by using the measured values of $\mathcal{V}_E(\pm V)$ to calculate $\Delta_E\mathcal{V}_E(V)$, from which we deduce a corrected fringe visibility given by $\mathcal{V}'_{EB}(V,I) = \mathcal{V}_{EB}(V,I)/[1 - \Delta_E\mathcal{V}_E(V)]$. This quantity is now simply expressed by Eq. (A11) (obviously, this correction is necessary only when studying V-odd terms).

The variations of $\mathcal{M}_B\Delta_E\mathcal{V}'_{EB}(V,I)$ give a test of the $\sum D_{-,+}$ term. We do not plot these results here because all the values are very small, in the $(-1$ to $+5) \times 10^{-3}$ range, with error bars near $\pm 2 \times 10^{-3}$, with one exception, for $I = \pm 19$ A (the visibility is then very low and some approximations of our calculations of the Appendix are no longer valid). The variations of $\Delta_B\mathcal{M}_E\mathcal{V}_{EB}(V,I)$ give a test of the $\sum D_{+,-}$ term. We do not plot these results here because all the values are also very small, in the $(-2$ to $+4) \times 10^{-3}$ range, with error bars near $\pm 2 \times 10^{-3}$. These two results prove that the $\sum D_{-,+}$ term and the $\sum D_{+,-}$ term are very small, in good agreement with our calculations, which predict that these terms should vanish if the contact potential terms are negligible.

Having verified that the $D_{-,+}$ terms are negligible, the quantity $\Delta_E\mathcal{V}'_{EB}(V,I)$ reduces to $\sum D_{-,-}/D_0$ [see Eq. (A12)]. The leading terms of $D_{-,-}$ given by Eq. (A8) are proportional to the Aharanov-Casher phase:

$$\Delta_E\mathcal{V}'_{EB}(V,I) \approx -\frac{\sum \varphi_{\mathrm{AC}} \sin(\phi_Z)}{\sum \cos(\phi_Z)}. \tag{13}$$

Thanks to our knowledge of the Zeeman phases [Eqs. (11)], we can evaluate all the terms of Eq. (13), and we compare its prediction to our measurements in Figs. 13 and 14. The good agreement, obtained without any fitted parameter, proves that the dominant V-odd effect is due to the AC phase shift, and confirms the validity of our calculations.

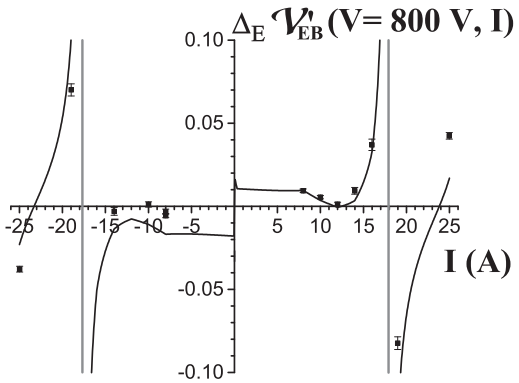

FIG. 13. Plot of $\Delta_E\mathcal{V}'_{EB}(V = 800$ V,I) as a function of the current I: the measured data points (squares) are compared to the result of our model (full line). The visibility, proportional to $D_0 = \sum \cos(\phi_Z)$, vanishes when $I \approx \pm 18$ A indicated by vertical lines: this induces a divergence of the prediction of our model, which uses a first-order calculation in $D_{\pm,\pm}/D_0$. Our model explains well the main variations of $\Delta_E\mathcal{V}'_{EB}(V,I)$, even if some imperfections appear clearly.

B. Tests involving the fringe phase

We first discuss the combination $\mathcal{M}_B\Delta_E\varphi_{EB}(V,I)$ given by

$$\mathcal{M}_B\Delta_E\varphi_{EB}(V,I) = -\frac{\sum N_{-,+}}{D_0}. \tag{14}$$

As $N_{-,+}$ is nonzero only if the contact potentials are not negligible, we expected this quantity to be negligible. $\mathcal{M}_B\Delta_E\varphi_{EB}$ is plotted as a function of I on Fig. 15 and as a function of V on Fig. 16. These experimental results are surprising: $\mathcal{M}_B\Delta_E\varphi_{EB}(V,I)$ is almost independent of the current I and it rapidly increases with the voltage V. The measured values are well fitted as the sum of two terms, one term in V and one in V^3 (odd powers of V have been chosen because this quantity is V odd).

Contact potentials can in principle explain nonzero values of $\mathcal{M}_B\Delta_E\varphi_{EB}$ (the calculation is made in Ref. [15]), but the predicted effect depends on the current I with divergences similar to those visible in Fig. 13, in complete disagreement

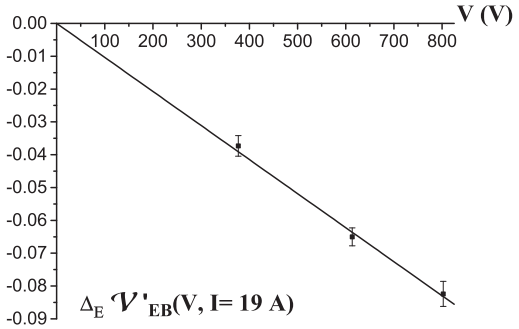

FIG. 14. Plot of difference of visibility for opposite V values, $\Delta_E\mathcal{V}'_{EB}(V, I = 19$ A), as a function of V. The current value $I = 19$ A, chosen close to the cancellation of $D_0 = \sum \cos(\phi_Z)$, enhances the sensitivity of the visibility to the AC phase. The measured values (squares) are well represented by a linear function of V, as predicted by our model.

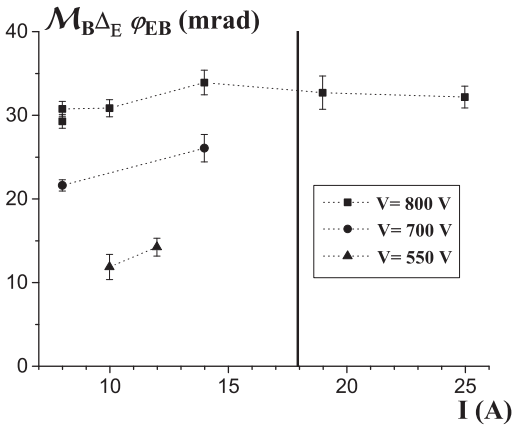

FIG. 15. Plot of the quantity $\mathcal{M}_B\Delta_E\varphi_{EB}(V,I)$ in radians as a function of the current I for several values of the voltage V applied to the capacitors. The dotted lines are simply connecting values measured for the same V values. The vertical line for $I \approx 18$ A indicates the place where the fringe visibility vanishes.

with the measurements plotted in Fig. 15. Moreover, the observed magnitude of $\mathcal{M}_B\Delta_E\varphi_{EB}(V,I)$ would require values of contact potentials that are ruled out by the measurements of $\mathcal{V}_E(V)$ and $\mathcal{V}_{EB}(V,I)$ previously presented. This effect is strange because $\varphi_{EB}(V,I)$ given by Eq. (3) is already a difference of phase shifts measured with and without the magnetic field, so that $\mathcal{M}_B\Delta_E\varphi_{EB}(V,I)$ must vanish when the applied magnetic field goes to zero: as a consequence, the independence of $\mathcal{M}_B\Delta_E\varphi_{EB}(V,I)$ from the current I cannot extend to $I \to 0$. However, if the transition occurs for instance when the laboratory field and the HMW field are comparable in magnitudes, it should be observed with a current I of the order of 0.1 A, a range of I values we have not studied.

We have investigated several possible explanations which were shown to be unsatisfactory for different reasons: usually, either the symmetry with respect to V and I reversals or the order of magnitude of the observed phase are not in agreement with our observations. Moreover, most attempts cannot explain why the effect is sensitive to the presence of the magnetic field but independent of its value in the studied range in Fig. 15.

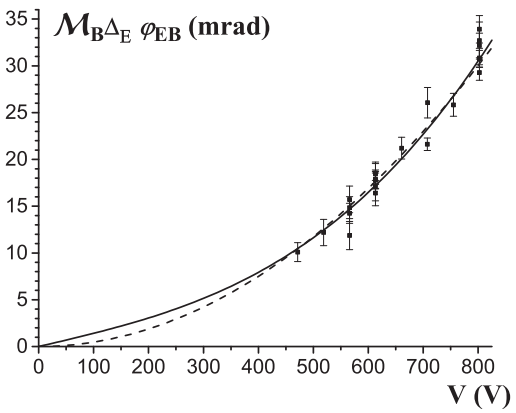

FIG. 16. Plot of the quantity $\mathcal{M}_B\Delta_E\varphi_{EB}(V,I)$ as a function of the voltage V applied to the capacitors for all the values of the current I in the HMW coil. The dotted line is a fit with a single V^3 term while the full line is a fit with a term in V and a term in V^3.

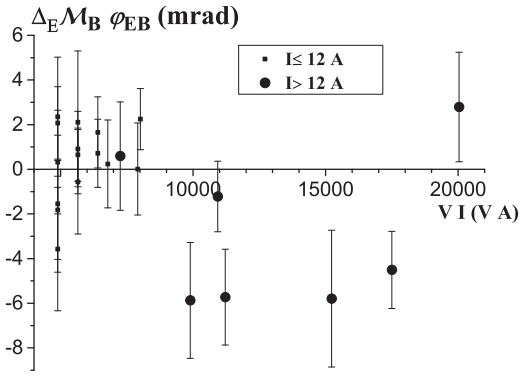

FIG. 17. Plot of the quantity $\Delta_B\mathcal{M}_E\varphi_{EB}(V,I)$ as a function of the product VI: the different symbols represent results for $|I| \leqslant 12$ A or $|I| > 12$ A.

We will not discuss here these failed explanations, for lack of space. The origin of this phase shift remains mysterious but because of its independence with regard to I, it can be easily eliminated by combining data with opposite I values.

We now discuss the quantity $\Delta_B\mathcal{M}_E\varphi_{EB}(V,I)$ which vanishes if the contact potentials are negligible. If they are taken into account, this quantity is given by [15]

$$\Delta_B\mathcal{M}_E\varphi_{EB}(V,I) \approx \frac{\sum \varphi_{AC}\langle\delta\varphi_{S,c}\delta\varphi_Z\rangle\cos(\phi_Z)}{\sum\cos(\phi_Z)}. \qquad (15)$$

Because of the presence of a contact potential term $\delta\varphi_{S,c}$, $\Delta_B\mathcal{M}_E\varphi_{EB}(V,I)$ is expected to be small, and we have not included higher-order terms in Eq. (15), because they should be even smaller. The measured values of $\Delta_B\mathcal{M}_E\varphi_{EB}(V,I)$ are plotted in Fig. 17, with different symbols for data points depending if $|I|$ is smaller or larger than 12 A. When $|I| \leqslant 12$ A, the measured values are very small and compatible with 0: in this range of I values, the Zeeman phases ϕ_Z are small because of the compensator, the systematic effects are weak, and the approximations done in our model are good. When $|I| > 12$ A, the Zeeman phases increase rapidly with $|I|$, and several effects decrease the accuracy of our model. First, the polynomial expansion of the Zeeman phases in powers of the current I is poorly convergent for some sublevels (see HMWI) while the systematic effects are very sensitive to the value of the Zeeman phases. Second, with increasing Zeeman phases, the systematic effects which involve the dispersion $\delta\varphi_Z$ increase (this point is discussed below). Finally, increasing Zeeman phases induce a rapid decrease of the visibility which cancels for $I \approx 18$ A, and higher-order terms in N_i/D_0 or D_i/D_0 are no longer negligible.

The tests on the fringe phase presented up to now have detected stray phase shifts not larger than 35 mrad. We end this part by considering the quantity $\mathcal{M}_E\varphi_{EB}$, which includes the largest stray phase shifts. $\mathcal{M}_E\varphi_{EB}(V,I)$ is an even function of the current I, because we have just shown that $\Delta_B\mathcal{M}_E\varphi_{EB}(V,I) = [\mathcal{M}_E\varphi_{EB}(V,I) - \mathcal{M}_E\varphi_{EB}(V,-I)]/2$ is negligibly small. $\mathcal{M}_E\varphi_{EB}$ is given by

$$\mathcal{M}_E\varphi_{EB}(V,I) = -\frac{\sum N_{+,+}}{D_0} \approx -\frac{\sum\langle\delta\varphi_{S,g}\delta\varphi_Z\rangle\sin(\phi_Z)}{\sum\cos(\phi_Z)}, \qquad (16)$$

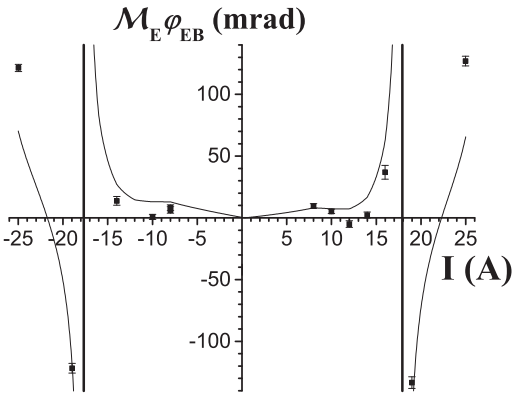

FIG. 18. Plot of the quantity $\mathcal{M}_E\varphi_{EB}(V,I)$ for $V = 800$ V, as a function of the current I. The points are measured values, the line is a best fit for all the measurements of $\mathcal{M}_E\varphi_{EB}$ (see discussion). As for Fig. 13, vertical gray lines indicate cancelation of the visibility.

where we have neglected higher-order terms [see Eq. (A8)]. The measured values of $\mathcal{M}_E\varphi_{EB}(V,I)$ for $V = 800$ V are plotted in Fig. 18. The Stark phase dispersion $\delta\varphi_{S,g}(y) \propto V^2$ has been characterized thanks to the study of $\mathcal{V}_E(V)$ (Sec. III C). The evaluation of the variations of $\delta\varphi_Z(y)$ with I is done at the expense of a supplementary approximation, assuming a rectangular profile for the field of the HMW coil along the atom trajectory (compare Fig. 2). It then becomes possible to perform a fit of the measured values of $\mathcal{M}_E\varphi_{EB}$ [taking into account the terms neglected in Eq. (16)]. The result of this fit is also shown in Fig. 18: a good agreement is found for the behavior of this quantity, and the fitted parameter values are compatible with the expected dispersion of $\delta\varphi_Z(y)$ along the atomic beam height according to the calculations of the magnetic field. This result confirms the importance of the spatial dispersion $\delta\varphi_Z(y)$ of the Zeeman phase shifts and it proves that the main systematic effects are due to these spatial phase dispersions.

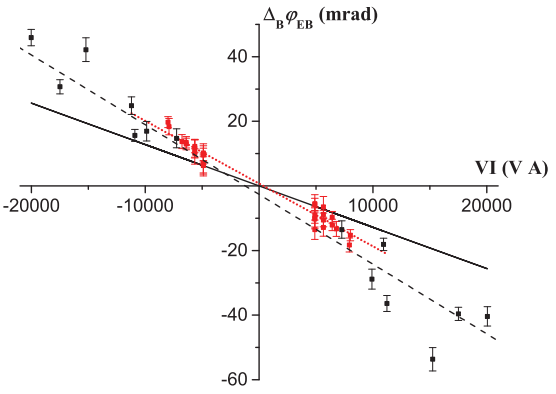

FIG. 19. (Color online) Measured values of $\Delta_B\varphi_{EB}(V,I)$ as a function of the product VI. The data points with $|I| \leqslant 12$ A are plotted in red as well as their fit represented by a dotted line. The data points with $|I| > 12$ A are plotted in black as well as their fit represented by a dashed line. The expected dependence of $\varphi_{\mathrm{HMW}}(V,I)$ on the VI product is represented by a black full line.

C. Conclusion concerning systematic effects

Here are the main results of our study of these effects:

(a) The effects of the spatial dispersions $\delta\varphi_{S,g}$ and $\delta\varphi_Z$ of the Stark and Zeeman phase shifts respectively are well identified.

(b) The effects of the the dispersion $\delta\varphi_{S,c}$ of the Stark phase due to contact potentials appear to be below our experimental sensitivity.

(c) Our model provides a qualitative understanding of the systematic effects for all values of the current I. The visibility decreases rapidly and vanishes for $|I| \approx 18$ A: this circumstance has been used to enhance the sensitivity to certain terms but clearly, as soon as $|I| > 12$ A, our model describing the systematic effects is less accurate.

(d) As the visibility presents a revival for $|I| \approx 23$ A with the Zeeman phases ϕ_Z being close to $\pm\pi$, we have made several series of measurements in this range of I values but we cannot expect our model to be accurate.

(e) We have observed an unexpected phase shift which is independent of the current I in the range 8–23 A and which is odd with respect to V reversal. We presently have no explanation for this effect and we continue our investigations into its possible sources. It may be either a systematic effect forgotten in our analysis or a fundamental physical effect, for instance such as the effects discussed by Anandan [18] but, as far as we can judge, either these fundamental effects are too small or they have not the correct symmetry with respect to V and I.

VII. MEASUREMENT OF THE HMW PHASE

We now use our knowledge of the stray phase shifts in order to eliminate their contributions to the measurement of the HMW phase. The HMW phase φ_{HMW} is proportional to the product VI, i.e., it is odd with respect to V and I reversals. The main contribution in the stray phase shifts to the measurements of φ_{EB} are even with respect to V and I, but because of the existence of a V-odd phase of unknown origin, we choose to use the I-odd character of φ_{HMW} to cancel the maximum amount of systematic effects. Accordingly, we plot in Fig. 19 the quantity $\Delta_B\varphi_{EB}(V,I)$ as a function of the product VI. We have used different symbols for the measurements depending on whether $|I|$ is smaller or larger than 12 A, and we have made separate fits of these two sets of data using $\Delta_B\varphi_{EB}(V,I) = \alpha VI + \beta$:

$$\begin{aligned} \alpha &= (-1.94 \pm 0.06) \times 10^{-6}\ \mathrm{rad/V\,A}, \\ \beta &= (7 \pm 4) \times 10^{-4}\ \mathrm{rad} \quad \text{if} \quad |\mathrm{I}| \leqslant 12\ \mathrm{A} \end{aligned} \tag{17}$$

and

$$\begin{aligned} \alpha &= (-2.16 \pm 0.14) \times 10^{-6}\ \mathrm{rad/V\,A}, \\ \beta &= (-26 \pm 19) \times 10^{-4}\ \mathrm{rad} \quad \text{if} \quad |\mathrm{I}| > 12\ \mathrm{A}. \end{aligned} \tag{18}$$

In both fits, the intercept β for $VI = 0$ is compatible with a vanishing value. The error bar on the slopes α is substantially smaller when $|I| \leqslant 12$ A than when $|I| > 12$ A: this is visible on the data which are more dispersed when $|I| > 12$ A. For both fits, the fitted slopes are larger (in modulus) than the predicted value $\varphi_{\mathrm{HMW}}(V,I)/(VI) = -(1.28 \pm 0.03) \times 10^{-6}$ rad/V A. The discrepancy is equal to

52% if $|I| \leqslant 12$ A and 69% if $|I| > 12$ A. Our model predicts that there are two contributions to $\Delta_B \varphi_{EB}(V,I)$:

$$\Delta_B \varphi_{EB}(V,I) = \varphi_{\mathrm{HMW}} - \frac{N_{-,-}}{D_0}. \tag{19}$$

$N_{-,-}$ given by Eq. (A8) is the product of the AC phase via the correlation terms. Thanks to the knowledge of the experimental defects, it is possible to evaluate all the terms involved in $N_{-,-}/D_0$. The only quantities not directly measured are the correlations $\langle \delta\varphi_d \delta\varphi_Z \rangle$ and $\langle \delta\varphi_d \delta\,(\varphi_Z)^2 \rangle$ which are evaluated from measurement of the correlation with $\delta\varphi_S$ replacing $\delta\varphi_d$, assuming that both effects are linear functions of y. The calculated value of $N_{-,-}/D_0$ never exceeds 3 mrad for the data set with $|I| \leqslant 12$ A, and we have made this correction to get $\varphi_{\mathrm{final}}(V,I)$ which is plotted in Fig. 3 of our Letter [3]. The fitted slope $\varphi_{\mathrm{final}}(V,I)/VI = (-1.68 \pm 0.07) \times 10^{-6}$ rad/V A is still too large but the discrepancy with the theoretical value is reduced to 31%.

VIII. CONCLUSION

A. Some remarks on the present experiment

We have described a measurement of the He-McKellar-Wilkens topological phase by atom interferometry. This experiment was feasible with our atom interferometer because the interferometer arms are well separated in space and the interferometer signal is intense, with a large fringe visibility, near 70%. The arm separation is needed in order to insert a septum between the two interferometer arms without any degradation of the signal. The signal intensity and the large value of the fringe visibility both contribute to enhance the phase sensitivity: its value achieved in practice near 25 mrad/$\sqrt{\mathrm{Hz}}$ is needed for the present measurement. The HMW phase shift is rather small, at most 27 mrad under our experimental conditions, and appears as the combination of four phase measurements for which 2000 s of data recording were needed to reduce the uncertainty near 3 mrad.

The analysis of the experiment was more complex than expected, because of stray phases. The complexity of the signal is due to several factors:

(a) The signal is the sum of the contributions of eight sublevels which are not exactly in phase because of the Zeeman phase shifts due to the slightly different values of the magnetic field on the two interferometer arms.

(b) We have built a compensator coil to produce an opposite gradient of the magnetic field at another place in the interferometer. The use of this compensator has been very fruitful as it has enabled us to apply substantially higher fields with a limited loss of fringe visibility. However the compensator produces a low field, so that it can correct only the part of the phase shifts due to linear Zeeman effect.

(c) The weights of the various F,m_F sublevels are functions of the laser frequency and power density in the standing waves used for atom diffraction. We had to control these parameters rather tightly in order to keep these weights almost equal and constant.

(d) The main phase shifts (diffraction phase shift, Stark and Zeeman phase shifts) present a dispersion with the atomic trajectory described in our calculations by the y coordinate. In the presence of several dispersed phase shifts, the visibility of the contribution of a given sublevel to the total fringe signal is better or worse, depending on whether the dispersions of the different phase shifts subtract or add their effects.

We have developed a model taking into account all these effects and this model has been very successful in explaining the variations of the observed phase shifts and visibility with the capacitor voltage V and the HMW coil current I. However, an extra phase has been observed and characterized: this phase is odd with the capacitor voltage V; it behaves roughly like V^3; it appears only when the magnetic field is applied but its value is independent of the magnetic field magnitude in a wide range. We continue our investigations to understand the effect which produces this phase. By combining measured phase shifts with opposite values of the current I, we have eliminated this phase and we have obtained a first measurement of the HMW phase shift. The observed effect is larger than its expected value by 69% if we use the data points with $|I| > 12$ A and only by 52% if we consider only the data points with $|I| \leqslant 12$ A. Finally, there is a small stray contribution of the Aharonov-Casher phase to the measured phase shift, and using our model, it was possible to evaluate this contribution and to correct the measured values accordingly. The discrepancy between our corrected measurements and the expected HMW phase shift is then reduced to 31%.

B. Possible improvements of this experiment

It is necessary to improve this experiment in order to reduce the uncertainty on the HMW phase shift. Here are the main possibilities:

(a) Reduction of stray effects by a better construction of the HMW interaction region. The present construction has two main defects: the difference of the capacitor thicknesses varies with the y coordinate and the septum does not coincide with the symmetry plane of the HMW coils. The construction of capacitors with a better controlled geometry is probably possible but quite difficult, because of the need to use a stretched septum. A better centering of the septum with respect to the HMW coils is probably rather easy and this would reduce substantially the Zeeman phase shifts which are the largest source of complication.

(b) Reduction of stray effects by optical pumping of the atomic beam. If all the atoms are in one F,m_F sublevel only, the signal is no more an average on the hyperfine sublevels populations. Moreover, the trajectory-averaged Zeeman phase shift can be exactly canceled by the compensator if the pumping is done in the $F = 2, m_F = +2$ (or -2) sublevel for which the Zeeman effect is exactly linear. As a consequence, this arrangement, which should reduce most of the stray phase shifts, is feasible with minor modifications of our setup and experiments are in progress.

(c) Reduction of stray effects by using another atom: this requires the development of a completely new atom interferometer with separated arms. Most of the difficulties are due to the paramagnetic character of lithium and an atom with a $^1S_0$ nondegenerate ground state (i.e., with a zero nuclear spin) would be ideal because there would be no Zeeman phase shift and no Aharonov-Casher phase shift. We may consider either a thermal beam of a light atom or a laser-cooled atomic source. In the case of a thermal beam,

the most obvious choice is ground-state helium, with which a very nice interferometer using diffraction by material gratings was developed by Toennies and co-workers (unpublished work quoted in [19]). Because helium electric polarizability is small ($\alpha_{He} \approx \alpha_{Li}/120$), larger electric and/or magnetic fields will be needed. Among atoms which have been laser cooled, magnesium, calcium, strontium, or ytterbium all have a $^1S_0$ ground state and at least one stable isotope with a nuclear spin equal to 0.

ACKNOWLEDGMENTS

We thank the laboratory technical staff for their help, A. Cronin for fruitful discussions, and G. Trénec, A. Miffre, and M. Jacquey for all the work done on our atom interferometer. We are greatly indebted toward CNRS INP, ANR (Grants No. ANR-05-BLAN-0094 and No. ANR-11-BS04-016-01 HIPATI), and Région Midi-Pyrénées for supporting our research.

APPENDIX: CALCULATION OF THE FRINGE SIGNAL

We describe here the main points of our calculation of the fringe signal from which we deduce the stray phase and the fringe visibility.

1. Some simplifying assumptions

The fringe phase φ is the sum of the diffraction phase φ_d, the Sagnac phase φ_{Sagnac} due to Earth's rotation, the Stark phase φ_S, the Zeeman phase $\varphi_Z(F,m_F)$, the HMW phase φ_{HMW}, and the Aharonov-Casher phase $\varphi_{\text{AC}}(F,m_F)$:

$$\varphi = \varphi_d + \varphi_{\text{Sagnac}} + \varphi_S + \varphi_Z(F,m_F) + \varphi_{\text{HMW}} + \varphi_{\text{AC}}(F,m_F). \tag{A1}$$

φ_d, φ_{HMW}, and $\varphi_{\text{AC}}(F,m_F)$ are independent of the atom velocity v; φ_{Sagnac} and φ_S vary like $1/v$ and $\varphi_Z(F,m_F)$ like $1/v^2$. These velocity-dependent phases are small [$\varphi_{\text{Sagnac}} \approx 0.65$ rad, $|\varphi_S| \lesssim 0.2$ rad, and $|\varphi_Z(F,m_F)| < 1.5$ rad when $|I| \leqslant 12$ A—only these data points will be retained for the final analysis]. As the parallel speed ratio $S_\parallel$ of the lithium beam is large, $S_\parallel \approx 9$, we may forget the velocity average and, as a consequence, the Sagnac phase φ_{Sagnac}, which is constant. We consider the spatial dispersion of φ_d, φ_S, and $\varphi_Z(F,m_F)$ only and we neglect this dispersion for φ_{HMW} and $\varphi_{\text{AC}}(F,m_F)$, because they are small, $|\varphi_{\text{HMW}}| < 27$ mrad and $|\varphi_{\text{AC}}(F,m_F)| < 70$ mrad, for our largest fields. The total phase dispersion $\delta\varphi$ is the sum of three terms only:

$$\delta\varphi = \delta\varphi_d + \delta\varphi_S + \delta\varphi_Z. \tag{A2}$$

From now on, the F,m_F dependence of φ_Z and φ_{AC} is not explicit and, for φ_d, φ_S, and φ_Z, we denote by ϕ_X the spatial average of φ_X given by $\phi_X = \langle\varphi_X\rangle = \int dy P(y)\varphi_X(y)$. The average over the F,m_F sublevels is taken with equal weights, $P(F,m_F) = 1/8$. This is a good approximation because, in the experiments devoted to the HMW phase measurement, we have kept χ small ($|\chi| < 0.03$) and randomly distributed around 0 (its main effect is to induce a supplementary dispersion of our phase measurements). With these approximations, following the discussion of Sec. IV of HMWI, the signal due to one F,m_F sublevel is given by

$$\begin{aligned} I(F,m_F) &= I_0\,[1 + \mathcal{V}_m\langle\cos(\varphi_m)\rangle]\,/8, \\ \mathcal{V}_m &= \mathcal{V}_0[1 - \langle(\delta\varphi)^2/2\rangle], \quad \varphi_m = \phi - \langle(\delta\varphi)^3/6\rangle \\ \text{with}\quad \phi &= \phi_d + \phi_S + \phi_Z(F,m_F) + \varphi_{\text{HMW}} + \varphi_{\text{AC}}(F,m_F) \\ \text{and}\quad \delta\varphi &= \delta\varphi_d + \delta\varphi_S + \delta\varphi_Z(F,m_F). \end{aligned} \tag{A3}$$

If we neglect nuclear magnetism, the F,m_F sublevels form four pairs with exactly opposite Zeeman energy shifts: three pairs of levels with the same m_F value and the pair $F = 2,m_F = \pm 2$. We label these pairs by an m_F value going from -1 to $+2$ and we denote by φ_Z the value of $\varphi_Z(F,m_F)$ for the sublevel $F = 2,m_F$.

2. Tutorial calculation

Because of numerous terms, these calculations are rather complicated, and we first present a tutorial calculation in which we cancel $\delta\varphi_d$ and $\varphi_{\text{AC}}(F,m_F)$, and we forget the cubic term in $\delta\varphi$. We first calculate the signal I_{pair} of a pair of sublevels:

$$\begin{aligned} \left[\frac{I_{\text{pair}}}{I_0/4} - 1\right]\Big/\mathcal{V}_0 &\approx \left[1 - \frac{\langle(\delta\varphi_S)^2\rangle + \langle(\delta\varphi_Z)^2\rangle}{2}\right] \\ &\quad\times \cos(\phi_Z)\cos(\phi_d + \phi_S + \varphi_{\text{HMW}} - \theta) \\ \text{with}\ \tan\theta \approx \theta &\approx \langle\delta\varphi_S\delta\varphi_Z\rangle\tan(\phi_Z). \end{aligned} \tag{A4}$$

The important point is the phase shift θ proportional to the correlation term $\langle\delta\varphi_S\delta\varphi_Z\rangle$ and this effect is due to the fact that the contributions of the two levels of the pair have different visibilities: the term $[1 - \langle(\delta\varphi_S + \delta\varphi_Z)^2\rangle/2]$ modifies these visibilities in a different way because the dispersions $\delta\varphi_S$ and $\delta\varphi_Z$ have the same sign for one level of the pair and opposite signs for the other one. Because of the $\tan(\phi_Z)$ factor, θ is very sensitive to the ϕ_Z value, especially when ϕ_Z is close to $\pi/2$.

3. Complete calculation

If we remove the approximations done in the tutorial example, we get the signal I_{tot} which has a form analogous to Eq. (A4):

$$\begin{aligned} \left[\frac{I_{\text{tot}}}{I_0} - 1\right]\Big/\mathcal{V}_0 &\approx \frac{1}{4}\,[D\cos(\phi_d + \phi_S + \varphi_{\text{HMW}}) \\ &\quad + N\sin(\phi_d + \phi_S + \varphi_{\text{HMW}})] \\ &\approx \frac{\sqrt{D^2 + N^2}}{4}\cos(\phi_d + \phi_S + \varphi_{\text{HMW}} - \theta) \\ \text{with}\ \tan\theta \approx \theta &\approx \frac{N}{D}. \end{aligned} \tag{A5}$$

The numerator N and the denominator D of the fraction giving θ are given by

$$\begin{aligned} D &= \left[1 - \frac{\langle(\delta\varphi_d + \delta\varphi_S)^2\rangle}{2}\right]D_0 + D_Z + D_{+/-}, \\ N &= \frac{\langle(\delta\varphi_d + \delta\varphi_S)^3\rangle}{6}D_0 + N_Z + N_{+/-} \end{aligned} \tag{A6}$$

with the following definitions:

$$
\begin{aligned}
D_0 &= \sum \cos(\phi_Z),\\
D_Z &= \sum \Bigg[-\frac{\langle(\delta\varphi_Z)^2\rangle}{2}\cos(\phi_Z)\\
&\quad + \frac{\langle(\delta\varphi_Z)^3 + 3\,(\delta\varphi_d)^2\,\delta\varphi_Z\rangle}{6}\sin(\phi_Z\Bigg)\Bigg],\\
D_{+/-} &= \sum [D_{+,+} + D_{-,+} + D_{+,-} + D_{-,-}],\\
N_Z &= \sum [\langle\delta\varphi_d\delta\varphi_Z\rangle\sin(\phi_Z) + \langle\delta\varphi_d(\delta\varphi_Z)^2\rangle\cos(\phi_Z)],\\
N_{+/-} &= \sum [N_{+,+} + N_{-,+} + N_{+,-} + N_{-,-}].
\end{aligned}
\tag{A7}
$$

In these equations, $\sum$ is the sum over the four pairs of levels labeled by the m_F value as defined after Eq. (A3) and this index is omitted everywhere. D_0 represents the effect of the Zeeman phase shifts ϕ_Z on the visibility, neglecting their spatial dispersion. D_B and N_B represent the effects of the dispersions of the diffraction phase shift $\delta\varphi_d$ and of the Zeeman phase shift $\delta\varphi_Z$. The effects of D_0 and D_B are independent of the application of the electric field. $D_{+/-}$ and $N_{+/-}$ are the sums of four terms which involve the simultaneous application of the electric and magnetic fields: the first index is the parity with respect to voltage reversal and the second index is the parity with respect to current reversal.

In Ref. [15], we have developed the calculations of the $D_{\pm,\pm}$ and $N_{\pm,\pm}$ terms including the contributions of the dispersion $\delta\varphi_{S,c}$ due to the contact potential (see HMWI) and the presence of this V-odd phase greatly increases the number of terms in these equations. As the contact potential terms appear to be extremely small, we do not take them into account in the present discussion but we refer the reader to Ref. [15] for a more complete discussion. With this simplification, $\delta\varphi_S$ is reduced to the geometrical defect term which is V even and the $D_{\pm,\pm}$ and $N_{\pm,\pm}$ terms are given by

$$
\begin{aligned}
D_{+,+} &= \left[\frac{\langle(\delta\varphi_S)^2\,\delta\varphi_Z\rangle}{2} + \langle\delta\varphi_S\delta\varphi_d\delta\varphi_Z\rangle\right]\sin(\phi_Z),\\
D_{-,+} &= D_{+,-} = 0,\\
D_{-,-} &= \left[-1 + \frac{\langle(\delta\varphi_d+\delta\varphi_S)^2\rangle + \langle(\delta\varphi_Z)^2\rangle}{2}\right]\\
&\quad\times\varphi_{\rm AC}\sin(\phi_Z) + \Bigg[\frac{\langle(\delta\varphi_Z)^3\rangle}{6} + \langle\delta\varphi_d\delta\varphi_S\delta\varphi_Z\rangle\\
&\quad + \frac{\langle(\delta\varphi_S)^2\,\delta\varphi_Z + (\delta\varphi_d)^2\,\delta\varphi_Z\rangle}{2}\Bigg]\varphi_{\rm AC}\cos(\phi_Z),\\
N_{+,+} &= \langle\delta\varphi_S\delta\varphi_Z\rangle\sin(\phi_Z) + \frac{\langle\delta\varphi_S\,(\delta\varphi_Z)^2\rangle}{2}\cos(\phi_Z),\\
N_{-,+} &= N_{+,-} = 0,\\
N_{-,-} &= [\langle\delta\varphi_S\delta\varphi_Z\rangle + \langle\delta\varphi_d\delta\varphi_Z\rangle]\,\varphi_{\rm AC}\cos(\phi_Z)\\
&\quad - \left[\frac{\langle(\delta\varphi_S+\delta\varphi_d)^3\rangle}{6} + \frac{\langle(\delta\varphi_S+\delta\varphi_d)\,(\delta\varphi_Z)^2\rangle}{2}\right]\\
&\quad\times\varphi_{\rm AC}\sin(\phi_Z).
\end{aligned}
\tag{A8}
$$

From these equations, it is easy to deduce the relative visibility and the phase shift of the interference fringes:

$$
\begin{aligned}
\mathcal{V}_r &= \frac{\mathcal{V}_m}{\mathcal{V}_0} = \frac{\sqrt{D^2+N^2}}{4} \approx \frac{D}{4},\\
\phi_m &= \phi_S + \varphi_{\rm HMW} - \theta, \quad \theta \approx N/D.
\end{aligned}
\tag{A9}
$$

We have used a third-order approximation of the sine and cosine functions in Eq. (23) of HMWI but we use only a first-order approximation to get $\theta \approx N/D$ and $\mathcal{V}_r \approx D/4$. This first-order approximation is good if $N \ll D$. For a practical use of these results, it will be necessary to assume that D_0 is considerably larger than the other terms appearing in D and that N is small with respect to D_0 so that we will further simplify the expression of $\theta \approx N/D_0$. We are going to use the following equations for the analysis of our experimental results:

$$
\begin{aligned}
\frac{\mathcal{V}_m(V,I)}{\mathcal{V}_0} &= \frac{1}{4}\left[\left(1 - \frac{\langle(\delta\varphi_S+\delta\varphi_d)^2\rangle}{2}\right)D_0 + D_Z + D_{+/-}\right],\\
\phi_m(V,I) &= \phi_S + \varphi_{\rm HMW} - \frac{\langle(\delta\varphi_S+\delta\varphi_d)^3\rangle}{6} - \frac{N_Z + N_{+/-}}{D_0}.
\end{aligned}
\tag{A10}
$$

4. Calculation of the phase shift and the visibility neglecting the effects of the laboratory magnetic field

To evaluate the visibility $\mathcal{V}_{EB}(V,I)$ and the phase $\phi_{EB}(V,I)$ defined by Eqs. (3), we use Eq. (A10) to calculate the terms corresponding to the different field configurations. As a first simplified approach, we consider that the laboratory magnetic field is homogeneous. In the case of field configurations for which $I = 0$, apart from canceling the Zeeman phase shifts, this also enables the neglect of the effect of the Aharonov-Casher phase. At first order in the stray terms, several cancellations appear:

$$
\begin{aligned}
\mathcal{V}_{EB}(V,I) &= 1 + \frac{D_{+/-}(V,I)}{D_0(V,I)},\\
\phi_{EB}(V,I) &= \varphi_{\rm HMW}(V,I) - \frac{N_{+/-}(V,I)}{D_0(V,I)}.
\end{aligned}
\tag{A11}
$$

Using the definitions of Eqs. (12), we separate the contributions in $D_{+/-}$ and in $N_{+/-}$ following their even or odd character with respect to V and I. Here are the results for the visibility:

$$
\begin{aligned}
\mathcal{M}_E\mathcal{V}_{EB} &= 1 + \left[\sum (D_{+,+} + D_{+,-})/D_0\right],\\
\Delta_E\mathcal{V}_{EB} &= \sum (D_{-,+} + D_{-,-})/D_0,\\
\mathcal{M}_B\mathcal{V}_{EB} &= 1 + \left[\sum (D_{+,+} + D_{-,+})/D_0\right],\\
\Delta_B\mathcal{V}_{EB} &= \sum (D_{+,-} + D_{-,-})/D_0.
\end{aligned}
\tag{A12}
$$

We fully separate the four $D_{\pm,\pm}$ terms by taking means or half differences of the above quantities:

$$
\begin{aligned}
\mathcal{M}_B\mathcal{M}_E\mathcal{V}_{EB} &= 1 + \left[\sum D_{+,+}/D_0\right],\\
\mathcal{M}_B\Delta_E\mathcal{V}_{EB} &= \sum D_{-,+}/D_0,
\end{aligned}
$$

$$\Delta_B \mathcal{M}_E \mathcal{V}_{EB} = \sum D_{+,-}/D_0,$$
$$\Delta_B \Delta_E \mathcal{V}_{EB} = \sum D_{-,-}/D_0. \quad \text{(A13)}$$

Similar combinations with the phase $\phi_{EB}(V,I)$ also enable the separation of the $N_{i,j}$ terms:

$$\begin{aligned} \mathcal{M}_B \mathcal{M}_E \phi_{EB} &= -N_{+,+}/D_0, \\ \mathcal{M}_B \Delta_E \phi_{EB} &= -N_{-,+}/D_0, \\ \Delta_B \mathcal{M}_E \phi_{EB} &= -N_{+,-}/D_0, \\ \Delta_B \Delta_E \phi_{EB} &= \varphi_{\mathrm{HMW}} - N_{-,-}/D_0. \end{aligned} \quad \text{(A14)}$$

5. Effect of the inhomogeneity of the laboratory magnetic field on the measurements

We now take into account the inhomogeneity of the laboratory magnetic field. Its main effect is to induce weak Zeeman phase shifts, and we neglect their spatial dispersions [$\delta J_0(y) = 0$]. This brings corrections only to the $D(0,0)$ and $D(V,0)$ terms, i.e., to the visibility terms in the field configurations for which $I = 0$. It is straightforward to calculate $D(0,0)$:

$$D(0,0) = \left[1 - \frac{\langle(\delta\varphi_d)^2\rangle}{2}\right] D_{0,B0}$$
$$\text{with} \quad D_{0,B0} = \left[1 + \cos(J_0) + 2\cos\left(\frac{J_0}{2}\right)\right]. \quad \text{(A15)}$$

When the electric field is applied, the residual Zeeman phase shifts are still present ($J_0 \neq 0$). With nonzero Zeeman phase shifts, the AC effect modifies the visibility independently of the presence of spatial phase dispersion $\delta\varphi(y)$: this modification is described by the leading term $-\varphi_{\mathrm{AC}}\sin(\phi_Z)$ in the expressions of $D_{-,-}$, Eqs. (A8). We thus obtain

$$D(V,0) = \left[1 - \frac{\langle(\delta\varphi_S + \delta\varphi_d)^2\rangle}{2}\right] D_{0,B0} + D_{AC,B0}$$
$$\text{with} \quad D_{AC,B0} = -\sum \varphi_{\mathrm{AC}} \sin(\phi_Z)$$
$$= -\varphi_{\mathrm{AC},B0}\left[\sin(J_0) + \sin\left(\frac{J_0}{2}\right)\right]. \quad \text{(A16)}$$

Here $\varphi_{AC,B0}$ is the AC phase of the $F = 2, m_F = 2$ sublevel in the presence of the laboratory magnetic field: this phase shift is proportional to the applied voltage V. In this way, we regain the results of Eq. (8) for the relative visibility $\mathcal{V}_E$, and we express the asymmetry $\Delta_E\mathcal{V}_E$ of the visibility with voltage reversal:

$$\mathcal{V}_E = 1 - \frac{\langle(\delta\varphi_S)^2\rangle}{2} - \langle\delta\varphi_S\delta\varphi_d\rangle + \frac{D_{\mathrm{AC},B0}}{D_{0,B0}},$$
$$\Delta_E\mathcal{V}_E = \frac{D_{\mathrm{AC},B0}(V)}{D_{0,B0}}. \quad \text{(A17)}$$

In the field configurations with $I \neq 0$, calculations of the type of Eqs. (A10) are not further modified. Therefore, the presence of the laboratory magnetic field brings a correction only to $\mathcal{V}_{EB}$ in Eqs. (A11), in the following form:

$$\mathcal{V}_{EB}(V,I) = 1 + \frac{D_{+/-}(V,I)}{D_0(V,I)} - \frac{D_{\mathrm{AC},B0}(V)}{D_{0,B0}}. \quad \text{(A18)}$$

[1] X.-G. He and B. H. J. McKellar, Phys. Rev. A **47**, 3424 (1993).
[2] M. Wilkens, Phys. Rev. Lett. **72**, 5 (1994).
[3] S. Lepoutre, A. Gauguet, G. Trénec, M. Büchner, and J. Vigué, Phys. Rev. Lett. **109**, 120404 (2012).
[4] S. Lepoutre, A. Gauguet, M. Büchner, and J. Vigué, preceding paper, Phys. Rev. A **88**, 043627 (2013).
[5] Y. Aharonov and A. Bohm, Phys. Rev. **115**, 485 (1959).
[6] Y. Aharonov and A. Casher, Phys. Rev. Lett. **53**, 319 (1984).
[7] A. Miffre, M. Jacquey, M. Büchner, G. Trénec, and J. Vigué, Eur. Phys. J. D **33**, 99 (2005).
[8] A. Miffre, Ph.D. thesis, Université P. Sabatier, 2005, http://tel.archives-ouvertes.fr/.
[9] S. Lepoutre, V. P. A. Lonij, H. Jelassi, G. Trénec, M. Büchner, A. D. Cronin, and J. Vigué, Eur. Phys. J. D **62**, 309 (2011).
[10] M. Jacquey, A. Miffre, M. Büchner, G. Trénec, and J. Vigué, Europhys. Lett. **77**, 20007 (2007).
[11] H. Wei, R. Han, and X. Wei, Phys. Rev. Lett. **75**, 2071 (1995).
[12] C. R. Ekstrom, J. Schmiedmayer, M. S. Chapman, T. D. Hammond, and D. E. Pritchard, Phys. Rev. A **51**, 3883 (1995).
[13] A. Miffre, M. Jacquey, M. Büchner, G. Trénec, and J. Vigué, Eur. Phys. J. D **38**, 353 (2006).
[14] We were helped by advice from A. Cronin (private communication).
[15] S. Lepoutre, Ph.D. thesis, Université Paul Sabatier, 2011, http://tel.archives-ouvertes.fr/.
[16] M. Puchalski, D. Kedziera, and K. Pachucki, Phys. Rev. A **84**, 052518 (2011); **85**, 019910(E) (2012).
[17] M. Jacquey, M. Büchner, G. Trénec, and J. Vigué, Phys. Rev. Lett. **98**, 240405 (2007).
[18] J. Anandan, Phys. Rev. Lett. **85**, 1354 (2000).
[19] A. D. Cronin, J. Schmiedmayer, and D. E. Pritchard, Rev. Mod. Phys. **81**, 1051 (2009).